Available free online at www.medjchem.com

Mediterranean Journal of Chemistry **2025**, 15(2), 218-232

Fixed-Bed Column Removal of Cyanide Using Graphene-Type Biochar: Influence of Operating Parameter

Djè Daniel Yannick [1], Yacouba Zoungranan [2, *], Kouadio Koffi Siméon [1], Kouassi Kouadio Dobi-Brice [1], Ekou Lynda [1] and Ekou Tchirioua [1]

[1] Laboratory of Thermodynamics and Physico-Chemistry of the Environment, NANGUI ABROGOUA University, 02 BP 802 Abidjan 02, Côte d'Ivoire

[2] Department of Mathematics, Physics, and Chemistry, Peleforo GON COULIBALY University, B.P. 1328 Korhogo, Côte d'Ivoire

Abstract: In this study, graphene-type biochar was synthesized from agricultural waste (oil palm seed shells of the hybrid dura x pisifera variety) and utilized as an adsorbent bed for cyanide removal from synthetic aqueous solutions. The material was characterized using X-ray diffraction (XRD), Fourier-transform infrared spectroscopy (FTIR), and scanning electron microscopy (SEM). Operational parameters, including column flow rate, initial cyanide concentration, and adsorbent mass, were examined. The Bohart-Adams, Thomas, and Young-Nelson models were applied to the experimental results. The synthesized adsorbent has a low moisture content, high ash content, and a neutral surface charge (pH 7.3). Its iodine number (Id) is 389.21 mg/g, indicating moderate porosity. The models showed that the theoretical saturation (N0) decreases with increasing mass and flow rate while these parameters remain favorable. The theoretical capacity (Q_{theo}) predicted by the Thomas model rises with both the initial concentration and the adsorbent mass. This study demonstrates the effective elimination of cyanide using the synthesized biochar, with strong predictive capabilities for column operation.

Keywords: Adsorption, cyanide, column, oil palm shells, graphene.

1. Introduction

Illegal gold mining in Côte d'Ivoire contributes to the country's economic growth, but it has negative impacts on water and soil quality. Cyanide, used for gold extraction, is often left untreated in cyanidation tanks [1]. Poor management of cyanide waste contaminates both surface and groundwater, harming aquatic ecosystems [2]. The acute and chronic toxicity of cyanide, along with its mobility and persistence, makes it a significant pollutant [3]. Finding effective solutions to prevent, reduce, and remediate cyanide pollution is a considerable challenge for the mining industry and Ivorian authorities. In response, innovative solutions are being explored. Various techniques exist for treating cyanide in water, including reverse osmosis [4], chemical oxidation [5], catalytic removal [6], photodegradation [6], electrochemical methods [7], and adsorption [8]. Adsorption, where molecules attach to the surface of a solid, is particularly favored for cyanide treatment due to its cost-effectiveness and the availability of adsorbent materials. Common adsorbents include activated carbon [9] and zeolites [10]. However, traditional carbon adsorbents have limitations due to the restricted internal adsorption sites [11], which has led to a growing interest in advanced synthetic adsorbents like graphene. Graphene, a two-dimensional material composed of a single layer of carbon atoms, exhibits enhanced adsorption capacity due to its hydrophilic nature and high charge density [12]. Yet, graphene-derived [13] nanoflakes can be unstable in water, tending to agglomerate, which reduces their effectiveness [11]. Additionally, the extraction process for graphite, the primary source of graphene, requires high temperatures, which increases costs and limits accessibility for some communities. This study is unique in its use of oil palm kernel shells, an agricultural waste, to synthesize graphene-enriched biochar. This innovative approach not only transforms biomass into a stable graphene-like material, addressing self-aggregation issues, but also promotes sustainability by utilizing waste. The objective of this research is to evaluate the effectiveness of cyanide removal through adsorption in a fixed-bed column containing this novel graphene-type biochar. Furthermore, the study aims to deepen the understanding of adsorption

**Corresponding author: Yacouba Zoungranan*
Email address: zoungranan@gmail.com
DOI: http://dx.doi.org/10.13171/mjc02506061828*zoungranan*

Received January 30, 2025
Accepted April 18, 2025
Published June 6, 2025

mechanisms and optimize operational parameters, highlighting the innovation and contributions of this research to the field of water treatment.

2. Material and Methods

2.1 Adsorbent synthesis

Oil palm (Elaeis guineensis) shells from the dura x pisifera hybrid variety were collected in Bonoua (5°16'N, 3°31'W), located southeast of Abidjan, Côte d'Ivoire (Fig. 1). The collected shells were transported to the laboratory for the synthesis of graphene-type biochar. The treatment involved several steps. First, the shells were crushed to separate the kernels. They were then washed with distilled water and dried in an oven (Memmert BM300, Schwabach, Germany) at 105°C for 48 hours. The synthesis of graphene-type biochar (BGp) followed the method of Xiao et al. [11]. with some modifications. In the first step, known as graphitization-activation, the shells were successively impregnated with solutions of ferric chloride ($FeCl_3$) and zinc chloride ($ZnCl_2$). The mixture was heated to 150°C while stirring on a hot plate (Nanbei, NB-H-Pro, Zhengzhou, China) until a viscous black substance formed. This substance was then placed in an oven at 80°C for 24 hours and subsequently heated in a muffle furnace (Nabertherm GmbH, Bremen, Germany) at 900°C for 1 hour, with a heating rate of 5°C/min. The solid residue obtained from the furnace was cooled, washed to achieve a neutral pH, dried, ground, and then sieved using a sieve (Saulas, Paris, France) to retain particles with diameters less than 100 µm, resulting in the graphene-type biochar (BGp) used in this study.

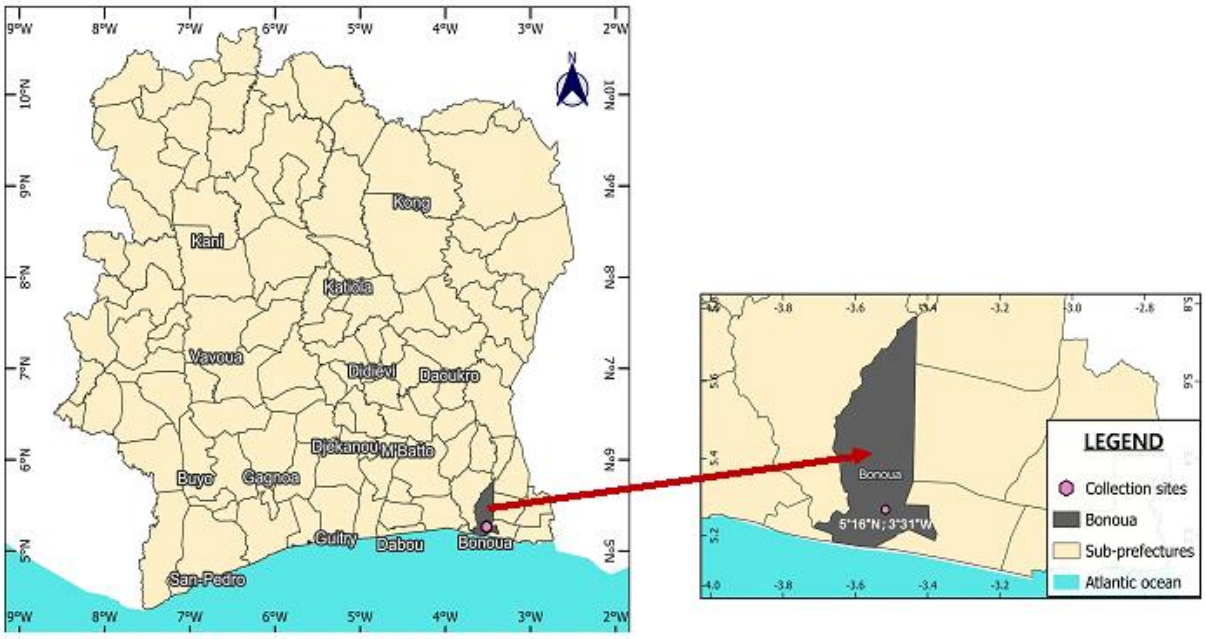

Figure 1. Location of Elaeis guineensis shell collection site

2.2 Adsorbent physico-chemical characterization

2.2.1 Moisture and Ash Content

An aliquot of BGp is placed in a crucible with an initial mass m_0. The crucible containing the BGp, with a combined mass of m_1 is then placed in an oven at 105 °C for 24 hours. After cooling, the mass m_2 of the crucible and BGp is determined before being transferred to a muffle furnace where the BGp is calcined at 650 °C for 1 hour. After calcination, the mass m_3 of the crucible and ash is determined.

The moisture content H of the BGp is calculated using the following equation (1):

$$H\,(\%) = \frac{m_1 - m_0}{m_2 - m_0} \times 100 \qquad (1)$$

The ash content A of the BGp is obtained using the following equation (2):

$$A(\%) = \frac{m_3 - m_0}{m_2 - m_0} \times 100 \qquad (2)$$

2.2.2 Zero Point of Charge (pHzpc)

To determine the pHzpc, a series of seven 250 mL beakers was used. In each beaker containing 0.5 g of BGp, a volume of 50 mL of a 0.1 M NaCl solution was added. The pH of each beaker was adjusted by adding either 0.1 M NaOH solution or 0.1 M HCl solution to achieve initial pH values (pH_i) of 2, 5, 7, 9, 11, and 13. The beakers were placed under magnetic stirring for 48 hours. After stirring and filtration, the final pH values (pH_f) of the solutions

were determined. The graphical representation of pHf−pHi=f(pHi) allows for the determination of the pHzpc of the BGp.

2.2.3 Iodine Number

A volume of 20 mL of a 0.1 N iodine solution is contacted with 0.05 g of BGp for 5 minutes. After filtration, 10 mL of the filtrate are titrated with a 0.1 N sodium thiosulfate solution in the presence of a few drops of starch indicator. A blank test is also conducted under the same conditions but without BGp. The iodine number Id, expressed in mg/g, is then calculated using the following equation (3):

$$Id = \left(\frac{V_0 - V}{m} \right) \times 12,69 \qquad (3)$$

With:

V_0 : Volume of thiosulfate used for the blank test
V: Volume of thiosulfate used for the sample with BGp
m: Mass of BGp

2.2.4-ray Diffraction (XRD) Analysis

The structural analysis of the BGp material was conducted using X-ray diffraction, employing a GBC-EMMA diffractometer (Braeside, Victoria, Australia) equipped with CuKα radiation (wavelength λ=0.154nm). The samples were analyzed over an angular range of 2θ from 0.15° to 91°, with a step size of 0.02°.

2.2.5 Scanning Electron Microscopy (SEM) Analysis

The morphology of the BGp was analyzed using a Zeiss SIGMA 300 scanning electron microscope (Graz, Austria).

2.2.6 Specific Surface Area

The specific surface area, pore volume, and average pore diameter of the BGp were determined using the nitrogen adsorption-desorption method based on the BET (Brunauer-Emmett-Teller) approach. These analyses were conducted using a Micromeritics Tristar II 3020 surface area and porosity analyzer (Georgia, USA).

2.2.7 Thermogravimetric (TGA) and Differential Thermal Analysis (DTA)

Thermogravimetric analysis (TGA) was performed using a Setsys Evolution 16 SETARAM analyzer (Pantélimon, Romania).

2.3 Fixed bed column adsorption studies

2.3.1 Experimental equipment

The experimental setup (Figure 2) consists of a cylindrical glass column measuring 37 cm in length, two reservoirs (one for the untreated solution and one for the treated solution), and a peristaltic pump. The column is fed with a cyanide solution through pumping, and the treated solution is collected at the column's outlet and stored in a reservoir, where regular samples are taken to analyze the residual cyanide concentration**.**

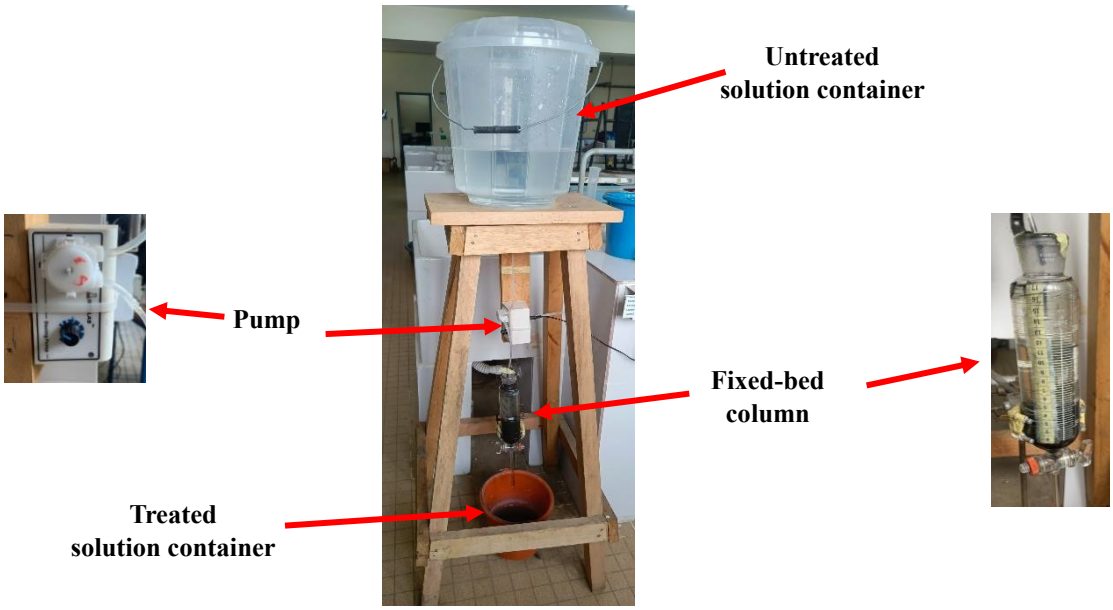

Figure 2. Experimental equipment.

2.3.2 Cyanide dosage

The analysis of residual cyanide at the column outlet is performed using the pyridine-pyrazolone method with cyanide-reactive powders from HACH (Loveland, USA). At regular intervals, a volume of 10 mL of the solution from the column outlet is collected and placed in a test tube. The Cyaniver 3 reagent powder is added, and the tube is capped and shaken vigorously for 30 seconds. After resting for 30 seconds, the Cyaniver 4 reagent is added, and the tube is shaken again. Following these two reagents, the Cyaniver 5 reagent is added and mixed under the same conditions. The tube is allowed to rest for 30 minutes, during which a bluish coloration appears, indicating the complexation of cyanide in the sample. The optical densities of the solutions are measured at 612 nm using a UV-visible spectrophotometer (WFJ-752, China).

The concentrations C_t are determined using the calibration curve established with potassium cyanide solution. The amount of cyanide adsorbed per gram of BGp at equilibrium (Q_{exp} in mg/g) is calculated using the following equation:

$$Q_{exp} = \frac{DC_0 \int_0^{t_s} f(t)\,dt}{m} \quad (4)$$

with $f(t) = 1 - \frac{C_t}{C_0}$ …. (5)

The function (f(t) is obtained through polynomial regression of the data points (C_t, t), where:

C_0 is the initial concentration of the solute (mg/L),
C_t is the concentration of the solute at time t (mg/L),
D is the flow rate (L/min),
t_s is the saturation time,
m is the mass of BGp (g).

The amount of cyanide adsorbed at equilibrium (Q_{exp}, in mg/g) can be calculated using the appropriate relationship derived from these parameters.

The results presented are the average of three independent repetitions

2.3.3 Mathematical models

The performance of the adsorption column has been studied using numerical models, including Bohart-Adams [14], Thomas [15], and Yoon-Nelson [16]. Each of these models is used to determine various operating parameters of the fixed bed column, such as theoretical adsorption capacity, saturation concentration of the adsorbent, and half-life of the adsorbent.

The Adams-Bohart model allows for the prediction of the saturation concentration of the bed (N_0). The following relationship expresses the linear form of the Bohart-Adams model:

$$\ln\left(\frac{C_t}{C_0}\right) = k_{BA}C_0 t - k_{BA}N_0\frac{z}{v} \quad \ldots\ldots \quad (6)$$

C_0 is the initial concentration of the solute (mg/L),
C_t is the cyanide concentration (mg/L),
K_{BA} is the Bohart-Adams kinetic constant (L/mg·min),
N_0 is the saturation concentration of the bed (mg/L),
v is the flow rate of the solution (cm/min),
z is the height of the adsorbing bed (cm).

The Thomas model enables the prediction of the theoretical adsorption capacity, Qtheo, of the column. The linear form of this model is expressed by the following equation (7):

$$\ln\left(\frac{C_0}{C_t} - 1\right) = \frac{k_{Th}Q_{the}m}{D} - k_{Th}C_0 t \quad (7)$$

Where:

C_0 is the initial concentration of the solute (mg/L),
C_t is the concentration of the solute (mg/L),
k_{Th} is the Thomas constant ($L \cdot mg^{-1} \cdot h^{-1}$),
m is the mass of the adsorbing bed (g),
Q_{theo} is the theoretical adsorption capacity (mg/g),
D is the flow rate ($L \cdot h^{-1}$).

The Yoon-Nelson model provides information on the time τ required to achieve 50% saturation of the adsorbing bed. The linearized form of this model is expressed by the following equation (8):

$$\ln\left(\frac{C_t}{C_0 - C_t}\right) = \tau k_{YN} - k_{YN}t \quad (8)$$

C_0 is the initial concentration of the solute (mg/L),
C_t is the concentration of the solute (mg/L),
k_{YN} is the Yoon-Nelson kinetic constant (min^{-1}),
τ is the time required to achieve 50% saturation of the column bed.

In this study, linear forms of the Thomas, Bohart-Adams, and Yoon-Nelson models were employed for analytical simplicity and to facilitate parameter comparison with other studies. However, nonlinear regression or dynamic modeling can provide predictions.

3 Results and Discussion

3.1 Characteristics of BGp

To better understand the behavior of the BGp adsorbent, a comprehensive study of its characteristics was conducted. Key results regarding the moisture content, ash content, density, and iodine number of this adsorbent are presented in the Table below:

Table 1. Systematic Characteristics of BGp.

Moisture content (H%)	Ash content (A%)	Density (g/cm³)	Iodine number (mg/g)	pHzpc
9.51 ± 0.10	11.74± 0.12	0,76 ± 0.013	389.21	7,3

The BGp adsorbent has a high ash content of 11.74%, which can be attributed to metal enrichment during its graphitization and activation process involving metal chlorides. Additionally, its low moisture content of less than 10% (9.51%) indicates that it is a highly adsorptive material; lower moisture levels mean that water is less likely to occupy adsorption sites. Furthermore, the density of BGp, measured at 0.76 g/cm³, suggests that it contains a greater amount of material per unit volume compared to materials with lower densities. The iodine number test revealed that the synthesized BGp has a very high specific surface area and good microporosity. However, this iodine value is lower than the 979 mg/g reported for activated carbon by Anderson [17] et al . This indicates that while BGp has developed microporosity, it does not reach the levels of conventional activated carbons. Additionally, the adsorption mechanisms may be influenced by other physicochemical properties of the material. Characterization of BGp also showed that its zero-charge point (pHzpc) is 7.3. This means that the surface of BGp is positively charged at pH values below this threshold and negatively charged at pH values above it.

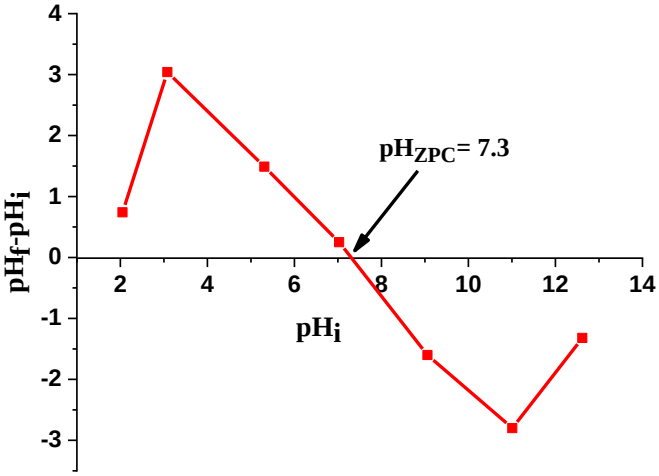

Figure 3. Zero Point of Charge (pHzpc)

Figure 4 shows the structural phases of BGp as determined by X-ray diffraction. The diffractogram shows a strong peak at 26.03°, characteristic of graphitic carbon. The intensity of these peaks indicates a high degree of graphitization, approaching a graphene-like structure [18].

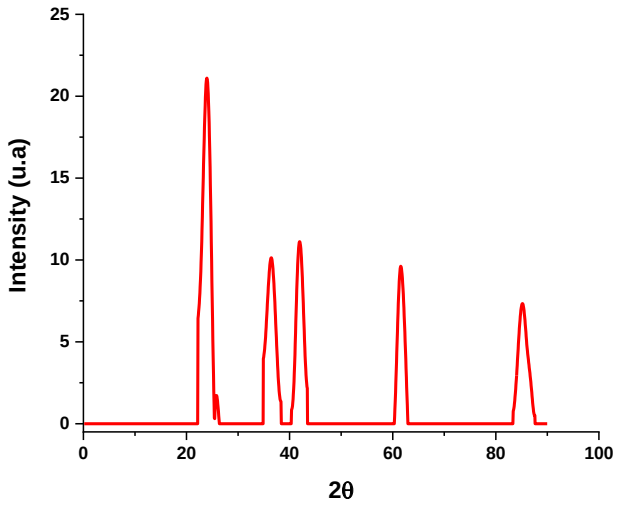

Figure 4. X-ray Diffraction (XRD) of BGp.

Microscopic analysis by SEM shows that the BGp material has a porous and heterogeneous structure at the nanoscale. The dark areas in the microscope represent voids and pores, while the lighter areas correspond to denser and more crystalline regions. This complex morphology, with its multi-scale porosity, is typical of adsorbent materials with a high specific surface area. It facilitates adsorption phenomena and interactions between the solid and species in solution [19].

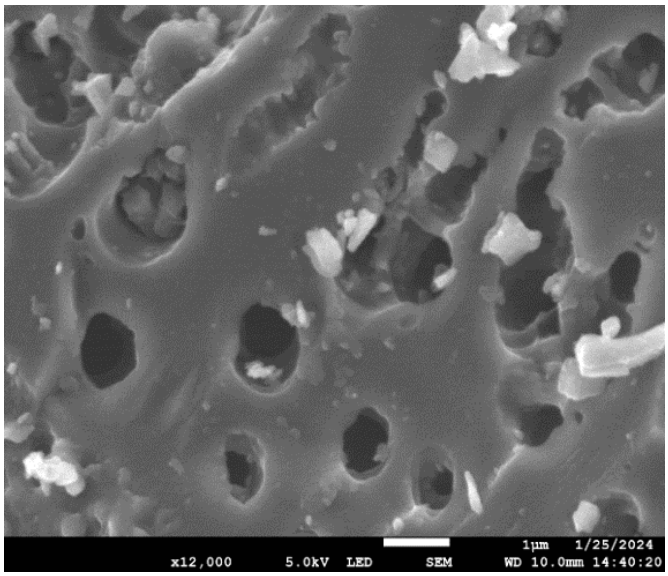

Figure 5. SEM image of BGp

The BET analysis showed that the BGp material has a specific surface area of 228.1969 m²/g, an average pore volume (according to the BJH model) of 0.017608 cm³/g, and an average pore diameter of 1.8990 nm. These results are consistent with those reported by Zhihao Zhang et al. [20], who found specific surface area values ranging from 140 m²/g to 432 m²/g for graphene-like materials.

Figure 6-a shows the pore size distribution calculated from the nitrogen adsorption isotherm using the BJH model, which enables the estimation of pore sizes within the material. Figure 6-b shows the hysteresis observed in the nitrogen adsorption-desorption isotherm for the same material, which is characteristic of its porous structure. This hysteresis provides additional information about the size, shape, and connectivity of the pores.

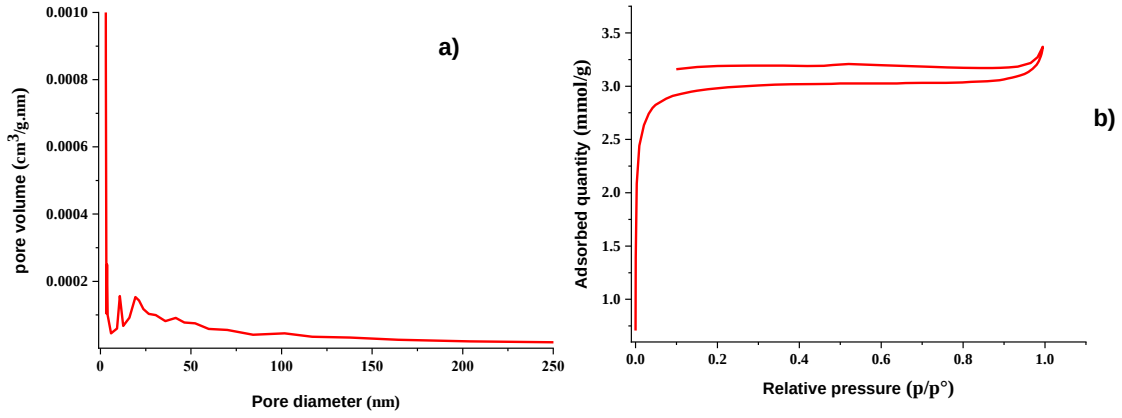

Figure 6. a) Pore size distribution for BGp extracted from nitrogen isotherms and b) nitrogen adsorption and desorption isotherms

The analysis of the pore size distribution, as illustrated in Figure 6-a, indicates an average pore size of approximately 1.8990 nm, which is below the 2 nm threshold. This verifies that the BGp material is, in fact, microporous. Moreover, the nitrogen adsorption-desorption isotherm exhibits an H4-type hysteresis loop, which is characteristic of porosity below 2 nm. This indicates microporosity, characterized by the reversible filling of micropores at low pressure, as well as slit-like pore shapes. The absence of a hysteresis loop characteristic of mesopores (2-50 nm) suggests that there is no

mesoporosity in this material [21]. The result of the Fourier transform infrared spectrometry analysis is shown in the following figure.

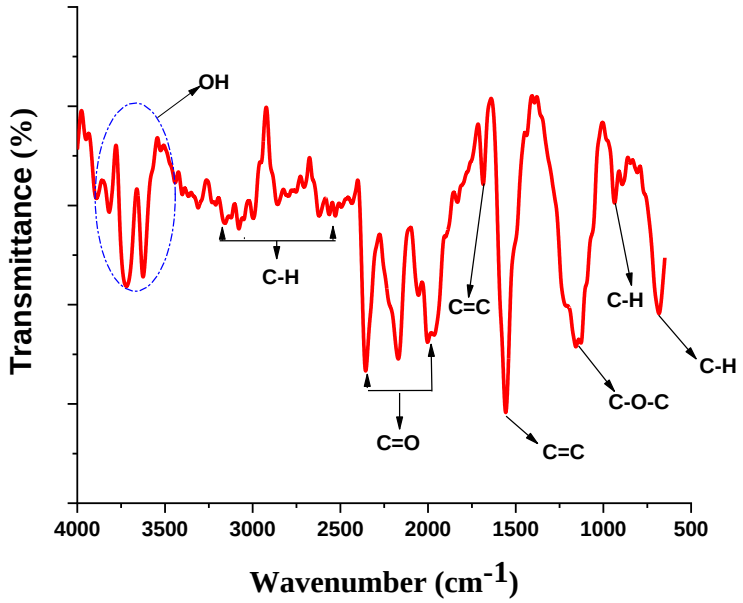

Figure 7. FTIR Spectrum of BGp

The band observed between 1560 and 1590 cm^{-1} is associated with the vibrations of C=C bonds in the aromatic network of graphene. The position and shape of this band indicate a high degree of graphitization, typical of biochar activated at high temperatures. Broadband absorption between 3400 and 3550 cm^{-1} indicates the presence of hydroxyl groups (O-H) on the surface of the biochar, which imparts hydrophilicity and enhances the material's reactivity [22]. The bands between 2850 cm^{-1} and 2920 cm^{-1} are indicative of aliphatic C-H bonds, suggesting that the biochar retains aliphatic fragments in addition to its graphenic structure. The band observed between 1720 and 1740 cm^{-1} is associated with carbonyl groups (C=O), such as those found in carboxylic acids, ketones, or esters, likely introduced during the chemical activation process. The bands between 1050 cm^{-1} and 1150 cm^{-1} correspond to the stretching vibrations of C-O-C bonds, indicating the presence of epoxy groups on the basal plane of graphene. The pronounced band at 1146 cm^{-1} suggests a substantial abundance of oxygenated functionalities, including ethers and alcohols, likely resulting from chemical activation with $FeCl_3$ and $ZnCl_2$. These groups enhance the polarity and chemical reactivity of the material. The band at 932.5 cm^{-1} indicates the presence of substituted aromatic cycles at positions 1, 2, and 4 in the structure, a likely consequence of the chemical activation process. Finally, the band at 680 cm^{-1} indicates the presence of tetra-substituted aromatic cycles, which impart distinctive properties to the biochar in terms of adsorption, catalysis, and conductivity.

Thermogravimetric analysis (TGA) enables the assessment of thermal stability, as well as the volatile matter and fixed carbon content, of graphene-type biochar. The figure below illustrates the TGA and DTG curves of BGp.

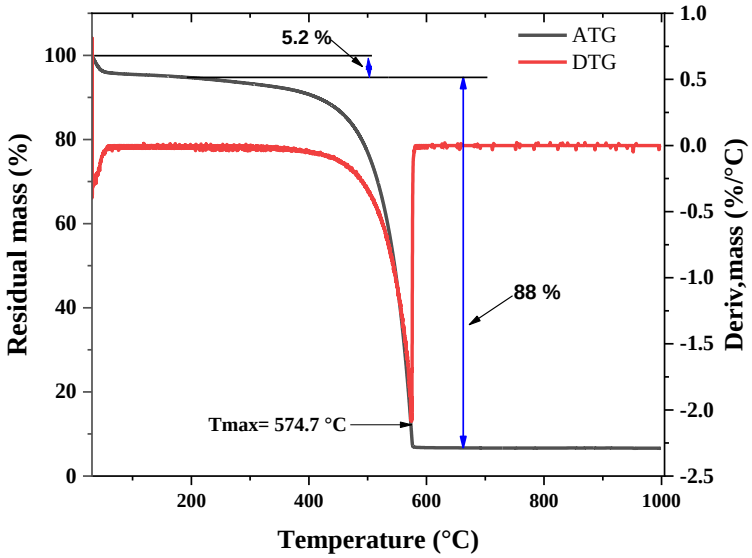

Figure 8. TGA and DTG Curves

The thermogravimetric analysis of the material indicates that a dehydration process occurs up to 200 °C. At this temperature, weakly bound water molecules are released, and the degradation of some extractive products is observed, as evidenced by a change in the slope of the curve. This dehydration process results in a mass loss of 5.2%. A distinct peak on the derivative thermogravimetric (DTG) curve indicates the degradation of natural polymers present in the oil palm seed shells. Following this, the residual solid matter from the dehydration process is defined as biochar. The temperature ranges up to 580 ℃ is associated with pyrolysis, leading to the formation of charcoal. The combustion step results in a significant mass loss of approximately 88% due to the degradation of volatile organic compounds. This phase is designated as passive pyrolysis, during which primary degradation of lignin occurs. Ultimately, the residual material remaining after treatment constitutes 6.8% of the total weight. The maximum mass loss was observed at 574.7 °C during the pyrolysis process [23].

The activation energy of the material is determined using the Coats-Redfern method, a commonly employed approach for calculating the activation energy (Ea) from thermogravimetric analysis (TGA) data. In establishing the equation, Coats-Redfern made the following assumptions:

$$\log\left[\frac{-\log(1-\alpha)}{T^2}\right]=\log\frac{AR}{\beta E_a}\left[1-\frac{2RT}{E_a}\right]-\frac{E_a}{2{,}303RT} \quad (9)$$

Where:

α is the degree of advancement of the reaction,
A is the pre-exponential factor,
R is the ideal gas constant (8.314 J/mol·K),
T is the absolute temperature (in K),
E_a is the activation energy (in J/mol),
β is the heating rate (in °C/min).
The degree of advancement of the reaction α is obtained through the following equation: $\alpha=\frac{W_0-W_t}{W_0-W_f}$ (10)

In this equation, W_0 represents the initial weight of the sample, W_t denotes the weight of the sample at a specified temperature, and W_f signifies the weight of the sample after the reaction.
The activation energy (Ea) is calculated by plotting a curve based on the following equation:

$$-\frac{\log(1-\alpha)}{T^2}=f\left(1000/T\right) \quad (11)$$

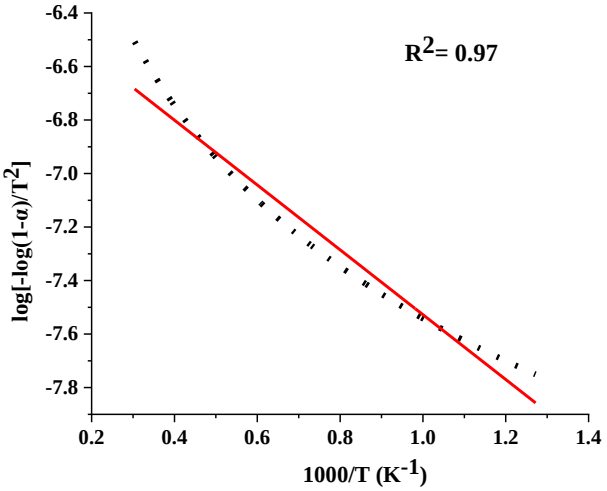

Figure 9. Determination of Activation Energy from TGA Analysis

The activation energy is derived from the slope of the curve using the following equation:

$$-\frac{E_a}{2,303R} = P \quad (12)$$

Where R is the ideal gas constant, and P is the slope of the curve.

The activation energy (Ea) of 23.20 kJ/mol indicates a moderate energy barrier that the material's molecules must overcome to initiate thermal degradation. This relatively low value suggests that only a minimal amount of thermal energy is required to start the degradation process. It implies that the degradation mechanism may involve relatively simple reaction steps, such as the breaking of weak chemical bonds, elimination reactions (like dehydration), and molecular rearrangements that require minimal energy.

As a result, the material exhibits moderate thermal stability, making it susceptible to degradation at relatively low temperatures, especially compared to materials with higher activation energies (Ea ≥ 50 kJ/mol). The reaction rate constant (k) for this activation energy of 23.20 kJ/mol will be higher than for materials with greater activation energies, as degradation occurs more rapidly at elevated temperatures due to accelerated kinetics. Furthermore, studies conducted by Bai et al. [25] have demonstrated relatively low activation energies, approximately 12.30 kJ/mol, alongside elevated reaction rate constants.

3.2 Influence of operating parameters

3.2.1 Absorbent Mass Effect

The impact of the BGp bed mass has been subjected to investigation, with the findings of this assessment presented in Figure 10.

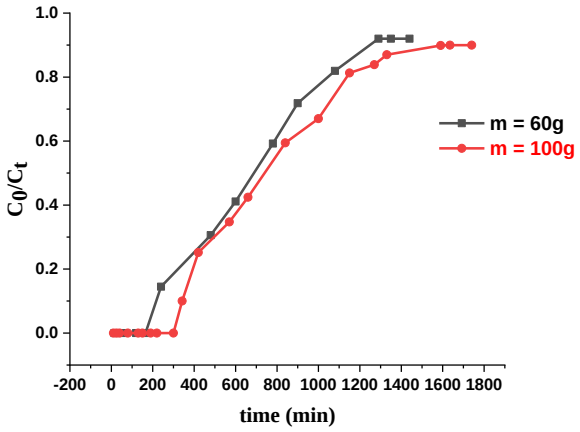

Figure 10. Curve Related to the Study of the Influence of BGp Mass on Cyanide Adsorption (D = 19 mL/min, C_0 = 1 mg/L, T = 25 °C, pH= 11)

As the mass of the BGp bed increases, the breakthrough time rises from 240 to 342 minutes, indicating an extension of the breakthrough period. This prolongation is attributed to the larger quantity of BGp, which provides an increased contact surface with the cyanide solution being treated. Consequently, the overall adsorption capacity increases, allowing for the retention of a greater quantity of cyanide. The increased availability of adsorption sites contributes to a reduction in the transfer rate from the liquid phase [26]. Thus, the multiplication of available sites delays the breakthrough time, defined as the point at which cyanide begins to exit the column without being retained. This augmented mass could facilitate the treatment of a greater volume of cyanide solution before it reaches saturation [27].

The equations of the different models were used to plot linear regression lines corresponding to the experimental results regarding the influence of BGp mass on cyanide adsorption in the column. These lines are illustrated in Figure 11.

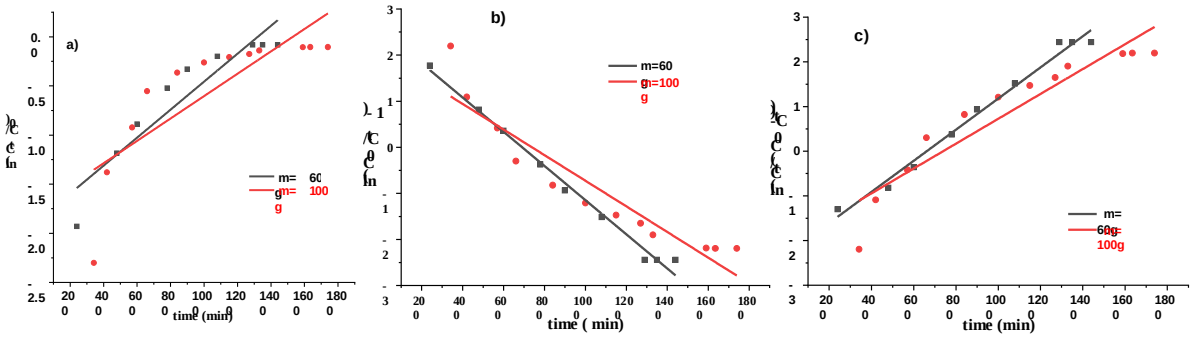

Figure 11. Linear Regression Lines Relating to the Influence of BGp Mass: a) Thomas model, b) Boart-Adams model, and c) Young-Nelson

The parameter values derived from the study of the impact of BGp mass on cyanide adsorption in a fixed-bed column are presented in Table 2.

Table 2. Model Parameters Relating to the Influence of Mass.

	Parameters									
	Thomas				**Bohart-Adams**			**Yoon-Nelson**		
	Q_{exp} (mg/g)	**K_{TH} (L/mg.h)**	**$Q_{théo}$ (mg/g)**	**R^2**	**K_{BA} (L/mg·min)**	**N_0 (mg/L)**	**R^2**	**K_{YN} (min^{-1})**	**T (min)**	**R^2**
m=60 g	22.85	0.00371	23.13	0.99	0.00142	982.4	0.87	0.00348	662.11	0.99
m=100 g	29.53	0.00278	30.43	0.88	0.00114	715.54	0.66	0.00278	739.51	0.88

The analysis of the data presented in the Table indicates that the kinetic constants of the Thomas, Bohart-Adams, and Yoon-Nelson models tend to decrease as the mass of the adsorbent in the column increases. This reduction in kinetic constants (kTH, kBA, and kYN) suggests that the rate of solute adsorption onto the adsorbent slows down with an increased amount of adsorbent [28]. This can be attributed to a decrease in the diffusion rate of the solute through a thicker adsorbent bed. As the mass of the adsorbent increases, the distance the solute must travel to reach available adsorption sites also increases, thereby slowing the adsorption process [29]. Furthermore, the data in the Table demonstrate that the saturation concentration (N0) declines as the mass of the adsorbent bed increases [30]. This suggests that with a greater quantity of adsorbent, the system reaches its maximum adsorption capacity in a shorter timeframe. In other words, a larger mass of adsorbent allows for a quicker approach to the limits of adsorption capacity [31]. Regarding adsorption capacities, the theoretical (Qthe) and experimental (Qexp) values of cyanide derived from the Thomas model are closely aligned, and both increase with the mass of the adsorbent bed. This can be attributed to the fact that adding more adsorbent increases the contact area between the solute (cyanide) and the adsorbent, thereby facilitating more efficient adsorption [32]. The analysis also shows that an increase in the mass of the adsorbent bed results in a longer time (τ) required to achieve 50% adsorption of the pollutants. The time needed to reach 50% adsorption of cyanide increases from 662.11 minutes to 739.51 minutes. This phenomenon can be

explained by the inverse relationship between the maximum adsorption capacity (N0) and the bed mass; as bed mass increases, N0 decreases. Consequently, the number of pollutants adsorbed at 50% of this reduced capacity is also lower, requiring a more extended period to reach this level of adsorption. Additionally, the distance the cyanide must traverse to reach equilibrium must be considered [31].

3.2.2 Concentration effect

The impact of cyanide concentration on a fixed BGp bed at a constant flow rate was also assessed. The outcomes of these experiments are presented in Figure 12.

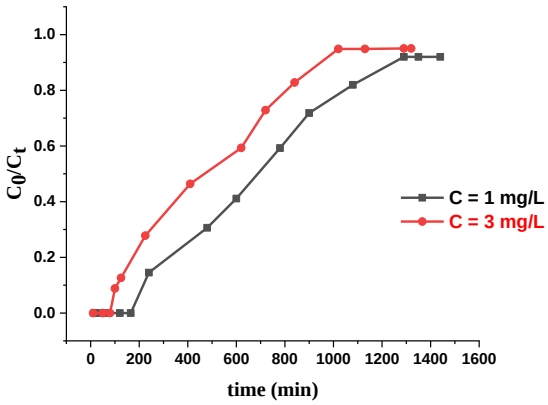

Figure 12. Curve Related to the Study of the Influence of Cyanide Concentration (D = 19 mL/min, m = 60 g, T = 25 °C, pH= 11)

The time required for a breakthrough decreases from 240 minutes to 100 minutes as the concentration factor is altered from high to low. A higher concentration factor allows the BGp to adsorb a greater quantity of cyanide. This places a greater demand on the fixed adsorption sites of the BGp, which are quickly saturated due to the high availability of the adsorbate. The concentration gradient facilitates the transfer of cyanide from the liquid phase to the surface of the BG, thereby increasing the efficiency of the column outlet process.

The equations derived from the models allowed for the generation of linear regression lines corresponding to the experimental results regarding the impact of cyanide concentration on the adsorption capacity of BGp. The lines mentioned above are presented in Figure 13.

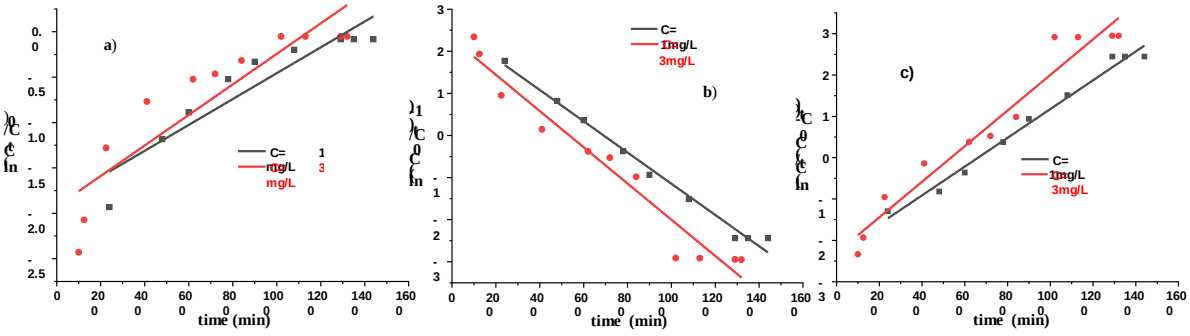

Figure 13. Linear Regression Lines Relating to the Influence of Cyanide Concentration: a) Thomas model, b) Boart-Adams model, and c) Young-Nelson

The parameters of the models derived from the study of the influence of cyanide concentration in a fixed-bed column of BGp are summarized in Table 4.

Table 4. Model Parameters Relating to the Influence of Cyanide Concentration.

	Parameters									
	Thomas				Bohart-Adams			Young-Nelson		
	Q_{exp} (mg/g)	K_{TH} (L/mg.h)	$Q_{théo}$ (mg/g)	R^2	K_{BA} (L/mg·min)	N_0 (mg/L)	R^2	K_{YN} (min^{-1})	T (min)	R^2
C=1 mg/L	22.85	0.00371	23.13	0.99	0.00142	982.4	0.87	0.00348	662.11	0.99
C= 3 mg/L	23.44	0.00144	24.60	0.95	0.00056	2549.94	0.81	0.00213	557.93	0.95

When the initial cyanide concentration increases from 1 mg/L to 3 mg/L, both the theoretical (Q_{theo}) and experimental (Q_{exp}) adsorption capacity values rise. This phenomenon can be attributed to an enhancement of the driving force behind the adsorption process. At higher concentrations, the concentration gradient between the liquid phase (solution) and the solid phase (adsorbent) becomes more pronounced, resulting in accelerated diffusion of the solute toward the adsorption sites. This enables more effective adsorption and a higher maximum adsorption capacity [33]. Furthermore, the increase in initial cyanide concentration leads to a significant rise in the saturation concentration (N0), which increases from 982.4 mg/L to 2549.94 mg/L. This increase in N_0 indicates that the maximum adsorption capacity of the system is significantly enhanced as the initial solute concentration rises. In other words, when the cyanide concentration in the solution is higher, the adsorbent can capture a greater quantity of pollutants before reaching saturation. Additionally, the time required for the adsorption process to reach 50% completion (τ) is reduced from 662.11 minutes to 557.93 minutes. This reduction can be attributed to the increased driving force for adsorption (the concentration gradient) at higher cyanide concentrations, allowing for more efficient solute adsorption and a shorter time to reach 50% of the maximum adsorption capacity [34]. Regarding the kinetic constants of the models, a reduction in these values (k_{TH}, k_{BA}, and k_{YN}) is observed as the initial cyanide concentration rises from 1 mg/L to 3 mg/L. This deceleration in adsorption kinetics can be ascribed to the accelerated saturation of the adsorbent's adsorption sites at elevated concentrations, which constrains the adsorption rate of cyanide. This observation is consistent with the findings of Chen Yunnen et al. [35] in their study on the removal of arsenate and arsenite from aqueous solutions.

3.2.3 Influence of Feed Flow Rate

The impact of the feed flow rate on cyanide adsorption has been investigated through the construction of curves that illustrate the variation of the ratio C_0/C_t as a function of time. The results of the evaluation of the influence of flow rate at constant m and C are shown in Figure 14.

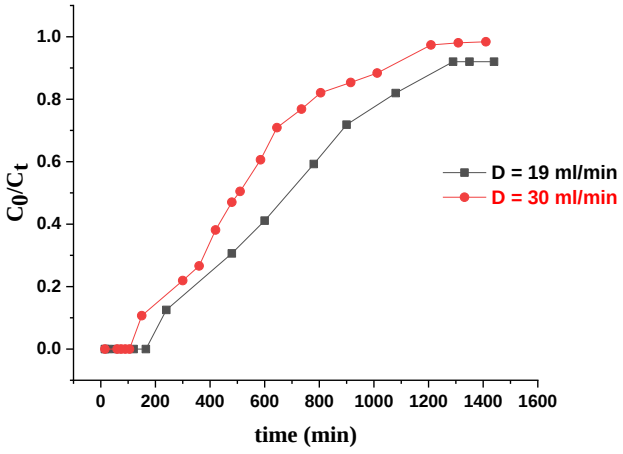

Figure 14. Breakthrough Curve Showing the Influence of Feed Flow Rate (C_0 = 1 mg/L, m = 60 g, T = 25 °C, pH= 11)

Analysis of the breakthrough curve revealed that at the lowest flow rate (19 mL/min), the breakthrough time was 240 minutes, whereas at the highest flow rate (30 mL/min), it was 150 minutes. Bed saturation occurs more rapidly at higher flow rates. An increase in flow rate leads to a reduction in breakthrough time and saturation time. As the flow rate increases, the contact time between the fluid and the BGp bed

decreases. This limits the transfer of cyanide to the BGp surface and facilitates the formation of an adsorption equilibrium [36].

The parameters of the Thomas, Bohart-Adams and Yoon-Nelson models, which relate to the study of the impact of feed rate on the BGp fixed-bed column, are presented in the Table below.

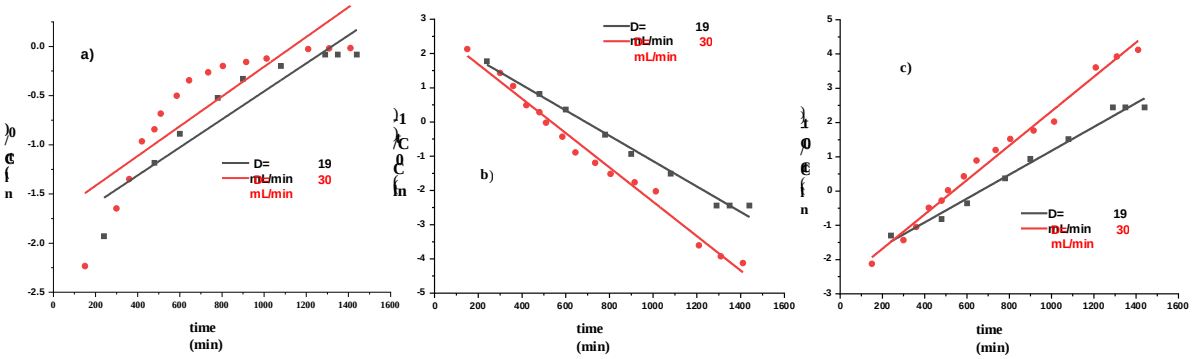

Figure 15. Linear regression lines for the effect of feed flow rate in the column: a) Thomas model, b) Bohart-Adams model, and c) Yoon-Nelson model.

The Table below illustrates the parameters of the Thomas, Bohart-Adams, and Yoon-Nelson models employed to investigate the impact of feed flow rate on the operation of the fixed bed column containing BGp

Table 5. Model Parameters Relating to the Influence of Feed Flow Rate.

	Parameters									
	Thomas model				**Bohart-Adams model**			**Young-Nelson model**		
	Q_{exp} (mg/g)	**K_{TH} (L/mg.h)**	**$Q_{théo}$ (mg/g)**	**R^2**	**K_{BA} (L/mg·min)**	**N_0 (mg/L)**	**R^2**	**K_{YN} (min^{-1})**	**T (min)**	**R^2**
D=19 mL/min	22.85	0.00371	23.13	0.99	0.00142	982.4	0.87	0.00348	662.11	0.99
D=30 mL/min	22.21	0.00502	22.05	0.99	0.00151	980.63	0.74	0.00502	535.10	0.99

Increasing the feed flow rate of the system from 19 to 30 mL/min results in notable changes in the parameters of the adsorption process. Firstly, the rate constants of the Thomas, Bohart-Adams, and Yoon-Nelson models show an increase. This increase indicates that the rate of the adsorption process accelerates at higher flow rates. At higher flow rates, the mass transfer of the solute to the adsorbent surface is favored, resulting in a faster adsorption process [37]. However, alongside this acceleration, there is a reduction in the quantity of the substance adsorbed, both in theoretical (Q_{theo}) and experimental (Q_{exp}) terms. This decrease in adsorption capacity can be attributed to a shorter contact time between the solute and the adsorbent at higher flow rates. Specifically, at elevated flow rates, the fluid spends less time in the adsorption column, thereby limiting the amount of solute that can be adsorbed [38]. These observations are further supported by the finding that the prediction time, which represents the time required for the system to reach saturation, also decreases as the feed flow rate increases from 19 to 30 mL/min. This reduction in predicted time reflects the acceleration of the adsorption process and the decline in adsorption capacity at higher flow rates. Finally, a slight decrease in the saturation concentration is observed, from 982.4 mg/L to 980.63 mg/L. This reduction in the maximum adsorption capacity of the system can be attributed to the kinetic and mass transfer effects induced by the increased feed flow rate, which hinder complete saturation of the adsorption sites.

4. Conclusion

This research highlights the effectiveness of graphene-like biochar, derived from oil palm seed hulls, in removing cyanide from wastewater by column adsorption. The results demonstrate that this material exhibits promising physicochemical properties and that various operational parameters, including flow rate and initial cyanide concentration, significantly influence its adsorption efficiency. Mathematical models, including those of Thomas and Bohart-Adams, were used to predict the adsorption capacity and other key characteristics. The study highlights the potential of biochar for treating contaminated water, paving the way for large-scale applications in industrial and agricultural settings. These results provide a solid basis for future research aimed at optimizing adsorption conditions

and exploring synergies with other technologies to improve the efficiency of water purification systems. Conducting real-life studies at gold mining sites to remove cyanide from post-extraction water, based on the parameters obtained in this study, would be particularly beneficial.

References

1. M. Gökelma, A. Birich, S. Stopic, B. Friedrich, A Review on Alternative Gold Recovery Re-agents to Cyanide, J Mater Sci Chem Eng, **2016**, 04, 8-17.
2. E. Kwaansa-Ansah, L. Amenorfe, E. Armah, F. Opoku, Human health risk assessment of cyanide levels in water and tuber crops from Kenyasi a mining community in the Brong Ahafo Region of Ghana, Int J Food Contam, **2017**, 4,16.
3. D. Jethava, P. Gupta, S. Kothari, P. Rijhwani, A. Kumar, Acute cyanide Intoxication: A rare case of survival, Indian J Anaesth, **2014**, 58, 312.
4. C. Goyburo-Chávez, J. Mendez-Ruiz, S. Jiménez-Oyola, P. Romero-Crespo, L. Gutierrez, P. Valverde-Armas, Pilot-scale reverse osmosis treatment of gold cyanidation effluent for the removal of cyanide, heavy metal(loid)s, and ionic species, Case Stud Chem Environ Eng, **2024**, 9, 100-688.
5. W. Han, H. Yang, L. Tong, Cyanide removal for ultrafine gold cyanide residues by chemical oxidation methods, Trans Nonferrous Met Soc China. **2022**, 32, 4129-4138
6. Y. Pan, Y. Zhang, Y. Huang, Y. Jia, L. Chen, H. Cui, Functional Ag-doped coralloid titanosilicate zeolite (CTS-Ag) for efficiently catalytic and photodegradative removal of free cyanides and copper/zinc-cyanide complexes in real wastewater, J Alloys Compd, **2022**, 926, 166-848.
7. M.K. Chegeni, A. Shahedi, AK. Darban, A. Jamshidi-Zanjani, M. Homaee, Simultaneous removal of lead and cyanide from the synthetic solution and effluents of gold processing plants using electrochemical method. J Water Process Eng, **2021**, 43, 102-284.
8. Y.D. Djè, Z. Yacouba, K. Kouassi, L.Ekou, T. Ekou, Cyanide removal by graphene-type oxidized biochar: kinetic study and adsorption isotherms, World J Adv Res Rev, **2024**, 22, 660-670.
9. J. Xia, R. Marthi, J. Twinney, A. Ghahreman, A review on adsorption mechanism of gold cyanide complex ontoactivation carbon, J Ind Eng Chem. **2022**, 111, 35-42.
10. I. Maulana, F. Takahashi, Cyanide removal study by raw and iron-modified synthetic zeolites in batch adsorption experiments, J Water Process Eng. **2018**, 22, 80-86.
11. X. Xiao, B. Chen, L. Zhu, J.L. Schnoor, Sugar Cane-Converted Graphene-like Material for the Superhigh Adsorption of Organic Pollutants from Water via Coassembly Mechanisms, Environ Sci Technol, **2017**, 51, 12644-12652.
12. J. George, D. Bhattacharyya, Graphene: an introduction in recent advances in Graphene and Graphene-Based Technologies, IOP Publishing, **2023**, 1, 1-24.
13. Y. Wei, G. Duan, Y. Huang, X. Han, C. Zhang, S. He, Application of magnetic graphene in the field of wastewater treatment, A review. J Water Process Eng, **2025,** 74, 107766.
14. S. Bakhta, Z. Sadaoui, N. Bouazizi, Cosme, O. Allalou, F. Derf, J. Vieillard, Successful removal of fluoride from aqueous environment using Al(OH) 3 @AC: column studies and breakthrough curve modeling, RSC Adv. **2024**, 14, 1-14.
15. H.C. Thomas, Heterogeneous Ion Exchange in a Flowing System, J Am Chem Soc, **1944**; 66, 1664-1666.
16. Y.H. Yoon, JH. Nelson, Application of Gas Adsorption Kinetics I. A Theoretical Model for Respirator Cartridge Service Life, Am Ind Hyg Assoc J. **1984** ;45, 509-516.
17. N. Anderson, H. Gu, R. Bergman, Comparison of Novel Biochars and Steam Activated Carbon from Mixed Conifer Mill Residues, Energies. **2021**, 14, 8472.
18. B. Chang, Y. Guo, Y. Li, Graphitized hierarchical porous carbon nanospheres: simultaneous activation/graphitization and superior supercapacitance performance,J. Mater. Chem. **2015**, 3, 9565-9577.
19. W.G. Lee, D.H. Kim, W.C. Jeon, S.K. Kwak, S.J. Kang, SW. Kang, Facile control of nanoporosity in Cellulose Acetate using Nickel (II) nitrate additive and water pressure treatment for highly efficient battery gel separators, Sci Rep. **2017**, 7, 1287.
20. Z. Zhang, H.C. Schniepp, D.H. Adamson, Characterization of graphene oxide: Variations in reported approaches, Carbon N Y. **2019**, 154, 510-521.
21. C. Schlumberger, M. Thommes, Characterization of Hierarchically Ordered Porous Materials by Physisorption and Mercury Porosimetry—A Tutorial Review, Adv Mater Interfaces. **2021**, 8.
22. B. Thangaraj, F. Mumtaz, Y. Abbas, D.H. Anjum, PR. Solomon, J. Hassan, Synthesis of Graphene Oxide from Sugarcane Dry Leaves by Two-Stage Pyrolysis, Molecules. **2023**, 28, 3329.
23. M. Uddin, S. Muntasir, F. Ahamed, H. Ahosan, Comprehensive characterization and kinetic analysis of coconut shell thermal degradation: Energy potential evaluated via the Coats-Redfern method, Case Stud Therm Eng. **2024,** 55, 104186.
24. A. Coats, J. Redfern, Kinetic Parameters from Thermogravimetric Data, Nature, **1964**, 201, 68-69.
25. H. Bai, N. Mao, R. Wang, Z. Li, M. Zhu, Q. Wang, Kinetic characteristics and reactive behaviors of HSW vitrinite coal pyrolysis:

A comprehensive analysis based on TG-MS experiments, kinetics models and ReaxFF MD simulations, Energy Reports. **2021**, 7, 1416-1435.
26. M. Mesfer, M. Danish, M. Khan, I. Ali, M. Hasan, A. Jery, Continuous Fixed Bed CO2 Adsorption: Breakthrough, Column Efficiency, Mass Transfer Zone, Processes. **2020**, 8, 1233.
27. G. Stavropoulos, G. Skodras, K. Papadimitriou, Effect of solution chemistry on cyanide adsorption in activated carbon, Appl Therm Eng, **2015**, 74, 182-185.
28. E. Gökırmak, M. Gülcan, Adsorption: basics, properties, and classification, Adsorption through Advanced Nanoscale Materials, Elsevier. **2023**, 3-21.
29. S. Mohamed, M. Abbas, M. Trari, Understanding the rate-limiting step adsorption kinetics onto biomaterials for mechanism adsorption control, Prog React Kinet Mech. **2024**, 49.
30. X. Yang, P. Liu, Yu H, Adsorption of heavy metals from wastewater using reduced graphene oxide titanate hybrids in batch and fixed bed systems, BMC Chem. **2025**, 19.
31. M. Marzbali, M. Esmaieli, Fixed bed adsorption of tetracycline on a mesoporous activated carbon: Experimental study and neuro-fuzzy modeling, J Appl Res Technol. **2017**, 15, 454-463.
32. T. Khan, T. Binti, M. Isa, Modeling of Cu(II) Adsorption from an Aqueous Solution Using an Artificial Neural Network (ANN), Molecules. **2020**, 25, 3263.
33. N. Rudi, M. Muhamad, L. Chuan, Evolution of adsorption process for manganese removal in water via agricultural waste adsorbent. Heliyon, **2020**, 6, 05049.
34. A. Ahmad, B. Hameed, Aziz N, Adsorption of direct dye on palm ash: Kinetic and equilibrium modeling, J Hazard Mater. **2007**, 141, 70-76.
35. C. Yunnen, W. Ye, L. Chen, G. Lin, N. Jinxia, R. Rushan, Continuous Fixed-Bed Column Study and Adsorption Modeling: Removal of Arsenate and Arsenite in Aqueous Solution by Organic Modified Spent Grains, Polish J Environ Stud. **2017**, 26, 1847-1854.
36. S. Biswas, U. Mishra, Continuous Fixed-Bed Column Study and Adsorption Modeling: Removal of Lead Ion from Aqueous Solution by Charcoal Originated from Chemical Carbonization of Rubber Wood Sawdust, J Chem. **2015**, 1, :1-9.
37. B. Omitola, M. Abonyi, K. Akpomie, F. Dawodu, Adams-Bohart, Yoon-Nelson, and Thomas modeling of the fix-bed continuous column adsorption of amoxicillin onto silver nanoparticle-maize leaf composite, Appl Water Sci. **2022**, 12, 94.
38. S. Muscarella, D. Trapani D, V. Laudicina, G. Mannina, Phosphorus recovery from ultrafiltered membrane wastewater by biochar adsorption columns: The effect of loading rates, Heliyon, **2024**, 10, 34659.